
**Liquid Crystals**
Publication details, including instructions for authors and subscription information:
http://www.informaworld.com/smpp/title~content=t713926090

# Electric field-induced fast nematic order dynamics

A. Amoddeo[a]; R. Barberi[b]; G. Lombardo[b]
[a] Mechanics and Materials Department University 'Mediterranea' of Reggio Calabria, Reggio, Calabria, Italy [b] CNR IPCF Liquid Crystal Laboratory, Physics Department, University of Calabria, Arcavacata di Rende, Italy

Online publication date: 15 January 2011

**To cite this Article** Amoddeo, A. , Barberi, R. and Lombardo, G.(2011) 'Electric field-induced fast nematic order dynamics', Liquid Crystals, 38: 1, 93 — 103
**To link to this Article: DOI:** 10.1080/02678292.2010.530298
**URL:** http://dx.doi.org/10.1080/02678292.2010.530298

*Liquid Crystals,*
Vol. 38, No. 1, January 2011, 93–103

Taylor & Francis
Taylor & Francis Group

# Electric field-induced fast nematic order dynamics

A. Amoddeo[a], R. Barberi[b] and G. Lombardo[b]*

[a] *Mechanics and Materials Department, University 'Mediterranea' of Reggio Calabria, Reggio Calabria, Italy;* [b] *CNR IPCF Liquid Crystal Laboratory, Physics Department, University of Calabria, Arcavacata di Rende, Italy*

(*Received 17 June 2010; final version received 5 October 2010*)

A strong electric field is able to induce transient and/or local biaxial states within a nematic calamitic phase, and the resultant nematic texture can be identified by the Landau–de Gennes $Q$-tensor theory. In this study we present a numerical $Q$-tensor model implemented with an adaptive moving-mesh finite element method, and this is able to describe the nematic order dynamics within a one-dimensional $\pi$-cell under the action of rapid electric pulses of different amplitudes. The proposed technique concentrates the grid points within regions of large $\nabla \boldsymbol{Q}$, keeping the total number of nodes in the domain constant in order to avoid waste of computational effort in areas where spatial order variability is low. Both the nematic order and the electric current flowing across the cell are strongly dependent on the amplitude of the applied electric field. The evolution of biaxiality allows not only monostable elastic distortions to be described, but also textural transitions between nematic states with different topologies.

**Keywords:** nematic liquid crystal modelling; orientational order; FEM; MMPDE; defects



## 1. Introduction

Thermotropic nematics consist of molecular core units, usually represented as simple rods having a cylindrical symmetry, which comprise a nematic phase, and are widely studied due to their role in the design of liquid crystal displays (LCDs). This type of application relies on the electro-optical effects exhibited by nematic materials, in which the application of an electric field induces textural distortions. The elastic behaviour framed in the classical theory [1, 2], in which the nematic phase is characterised by uniaxial order, is described by both the director, **n**, and the scalar order parameter, $S$ [3]. This theory takes account of the well known Freedericksz transition [3], which may be expressed as follows: if an electric field is applied to a nematic LC, the starting texture, prescribed by suitable boundary surfaces, can be elastically distorted into a topologically equivalent texture and the LC returns to its original configuration when the external field is switched off, showing a *monostable* behaviour. Fast monostable LCDs based on the Freedericksz transition meet all the main applicational requirements, such as displays for computers or TVs, but they are not suitable for novel applications such as e-paper-like displays, an emerging technology relevant, for instance, in e-book readers. In this case, the most important property is the intrinsic memory of the display, which has to save the last screen for a long period without requiring to be refreshed or receiving input from an external power source. This requires at least a *bistable* behaviour [4].

The classical theory fails to describe correctly the experimental evidence for *bistable* or *multistable* behaviour in nematic LCs, but these effects are more common than was considered only a few years ago. They can be observed when nematic textures are subjected to a high degree of frustration, as in the case of transitions induced by nano-confinement [5], of order reconstruction phenomena [6–13] or, even more importantly, of molecular order variation within the core of a nematic defect [14]. As a consequence, when the nematic order is strongly distorted over a scale of length comparable to the biaxial nematic coherence length, $\xi_b$, a transient local biaxial nematic states arises [15]. In these cases, a full Landau–de Gennes $\boldsymbol{Q}$-tensor description is mandatory to correctly describe the strong nematic distortions arising inside the calamitic phase [13, 16], and in particular the *order reconstruction* dynamics. This latter mechanism allows the connection of two topologically non-equivalent nematic textures by use of a fast electric field [6–13], and takes place whenever two conflicting uniaxial states are recomposed in space through a large number of transient biaxial states. From a mathematical point of view this implies the exchange of two of the $\boldsymbol{Q}$ eigenvalues, occurring when they approach each other and are finally exchanged, without involving any rotation of the $\boldsymbol{Q}$ eigenframe. The eigenvectors, $\boldsymbol{e}_1$, $\boldsymbol{e}_2$, and $\boldsymbol{e}_3$, of $\boldsymbol{Q}$ are the directions of the preferred molecular orientations, and the associated eigenvalues, $\lambda_1$, $\lambda_2$, and $\lambda_3$, represent the degree of order along each of the corresponding directions [17]. Calamitic nematic

*Corresponding author. Email: giuseppe.lombardo@cnr.it

ISSN 0267-8292 print/ISSN 1366-5855 online

DOI: 10.1080/02678292.2010.530298
http://www.informaworld.com

materials can exhibit three different phases (isotropic, uniaxial and biaxial), and these are distinguished by consideration of $\lambda_1$, $\lambda_2$, and $\lambda_3$. In the isotropic phase, the calamitic molecules do not present any orientational order and the optical behaviour is similar to that of an isotropic fluid. The uniaxial nematic phase presents a unique optical axis, described by the eigenvector associated with the maximum eigenvalue, $\lambda_{\max}$, giving the scalar order parameter, $S = (3/2)\ \lambda_{\max}$, while the remaining two eigenvalues are equal. In the biaxial nematic phase, however, all three eigenvalues are different. In this case, the coexistence of topologically non-equivalent uniaxial nematic textures, forbidden in the Frank–Oseen model, allows *bistable* or *multistable* states [18].

The modelling of the $\boldsymbol{Q}$-tensor dynamics leads to a system of coupled, strongly non-linear, partial differential equations (PDE), whose analytical solution can be obtained only in particular cases. Moreover, the physical problem lies in the micrometer length scale, whereas the biaxial order, according to $\xi_b$, decays in the nanometer scale length. It follows that in order to obtain reliable profiles of the order tensor, $\boldsymbol{Q}$, highly efficient numerical methods are needed. Using the finite element method (FEM) [19–20] to model the $\boldsymbol{Q}$-tensor dynamics, the integration domain is divided into elements on which nodes the solution is found, while inside each element the variation of $\boldsymbol{Q}$ is interpolated using suitable shape functions. The selection of an appropriate discretisation for the integration domain is always crucial, particularly in frustrated nematic systems where the order of the gradient, and the local transient biaxiality, become important. Adaptive grid techniques, both static (h- or p-type) or dynamic (r-type), allow improvements in resolution and computational savings with respect to techniques based on uniform discretisations [21–23]. Static h-type remeshing methods rely on the insertion of extra mesh points in order to satisfy tolerance requirements, whereas static p-type techniques keep the number of nodes constant, increasing the order of the polynomial used to represent the solution within each element. On the other hand dynamic r-type techniques, also known as *moving mesh* techniques, keep constant the nodal connectivity and number of mesh points inside the domain, moving them towards regions where more details are required. Unfortunately, static remeshing techniques can lead to an undesirably huge quantity of points, both memory and time consuming (h-type), or can be limited by smoothness requirements (p-type).

FEM has in the past been employed to model LC systems [13, 24–26] using static remeshing techniques. Ramage and Newton [27] used a dynamic r-type method in order to reproduce earlier numerical results obtained by the finite difference method [6]. In a recent study [28] we have performed one-dimensional numerical simulations on a $\boldsymbol{Q}$-tensor model of a nematic confined in a $\pi$-cell, obtaining numerical solutions of the PDE system by FEM by use of a novel numerical moving mesh PDE (MMPDE) technique. In our study we addressed the algorithm optimisation, seeking a monitor function suitable for the description of the phenomenon. The numerical calculations were performed using an adaptive r-type algorithm, which concentrates the grid points in regions of large $\nabla \boldsymbol{Q}$, while keeping the total number of the nodes in the domain constant. In addition, two different monitor functions have been compared, each having different characteristics of mesh points clustering inside the integration domain: the popular, arc–length (AL) monitor function, and one tested by Beckett and Mackenzie (BM) [30], and belonging to the type of monitor functions proposed by Huang et al. [30]. Our findings showed that the best results are obtained using the BM monitor function, as these ensure a more uniform nodal distribution inside core regions where steep solution variations are located, giving an improvement in resolution. In addition, the BM monitor function has proved to be self-regulating and is naturally smoothed, and requires fewer smoothing loops than the AL function. This provides a substantial reduction in arbitrary external intervention, indicating the BM rather than the AL algorithm as recommended for solving problems regarding nematic order reconstruction phenomena.

In the present study, we have applied the BM algorithm of our MMPDE numerical technique to a nematic condition confined within a $\pi$-cell with *symmetric* anchoring conditions in order to monitor the nematic order dynamics as a function of the amplitude of the applied electric field. In addition, we have performed a numerical evaluation of the electric current flowing during the application of the electric field, since this it is very sensitive to changes of nematic order, and it may be applied to experimental observations [7–9]. Our aim has been to extend numerical simulations to nematic systems which are subjected to different degrees of frustration, gaining new insights from the calculations.

## 2. Model theory

In general, the order of a nematic liquid crystal texture may be described globally by the symmetrical, second-rank, traceless tensor in the orthonormal basis of its eigenvectors $\{\boldsymbol{e_1}, \boldsymbol{e_2}, \boldsymbol{e_3}\}$,

$$Q = \sum_{i=1}^{3} \lambda_i e_i \otimes e_i. \tag{1}$$

The order tensor can be expressed in terms of five independent parameters, $q_i$, $i \in [1,5]$, corresponding to the degrees of freedom of a nematic molecule,

$$Q = \begin{pmatrix} q_1 & q_2 & q_3 \\ q_2 & q_4 & q_5 \\ q_3 & q_5 & -q_1 - q_4 \end{pmatrix}. \tag{2}$$

The description of nematics in biaxial configurations requires a complete representation of the above equations, since $\boldsymbol{Q}$ is a tensor field varying inside our domain. In the Landau–de Gennes framework, the free energy density $F$ is expressed in powers of $\boldsymbol{Q}$, assuming its dependence on small $\boldsymbol{Q}$ distortions. A complete review is given, for example, in references [3] and [17]. The $\boldsymbol{Q}$-tensor response of a nematic to an external field can be determined by means of variational principles, minimising the free energy density functional within the cell containing the LC, given by

$$F = \int_V (F_d + F_t + F_e) dV + \int_\sigma F_\sigma d\sigma \tag{3}$$

in which $F_t$, $F_e$ and $F_d$ are, respectively, thermotropic, electric and elastic contributions to the free energy density, and $\sigma$ is the boundary surface of the domain volume, $V$. Considering infinite anchoring strength, and therefore Dirichlet boundary conditions for the LC, and neglecting surface contribution to the energy density since the boundary conditions are fixed, we arrive at

$$F_t = F_t[Q], F_e = F_e[Q, \nabla Q], F_d = F_d[Q, \nabla Q], \tag{4}$$

$$F_t = a \operatorname{tr}\left[\mathrm{Q}^2\right] - \frac{2\mathrm{b}}{3} \operatorname{tr}\left[\mathrm{Q}^3\right] + \frac{\mathrm{c}}{2}\left[\operatorname{tr}\left[\mathrm{Q}^2\right]\right]^2, \tag{5}$$

where $a = \alpha[T - T^*] = \alpha \Delta T$, and $\alpha > 0$. $b$ and $c$ are temperature dependent but approximate to constants, and $T^*$ is the supercooling temperature [3] at which the isotropic state of the nematic becomes unstable,

$$F_e = -\frac{\varepsilon_0}{2}\left[\varepsilon_i |\nabla U|^2 + \varepsilon_a \nabla U \cdot Q \nabla U\right] + \bar{e}[\nabla \cdot Q] \cdot \nabla U, \tag{6}$$

where $U$ is the electric potential, $\varepsilon_i$ and $\varepsilon_a$ are the isotropic and the anisotropic dielectric susceptibilities, respectively,

$$\varepsilon_i = \frac{(\varepsilon \parallel + 2\varepsilon\perp)}{3}, \varepsilon_a = \frac{(\varepsilon \parallel - \varepsilon\perp)}{Seq}, \tag{7}$$

$\varepsilon_{||}$ and $\varepsilon$ are the parallel and the perpendicular dielectric nematic constants,

$$\bar{e} = \frac{e_{11} + e_{33}}{2S_{eq}}, \tag{8}$$

$e_{11}$ and $e_{33}$ are the splay and bend flexo-electric coefficients, and

$$S_{eq}[\Delta T] = \frac{b}{4c}\left[1 + \sqrt{1 - \frac{24ac}{b^2}}\right], \tag{9}$$

is the equilibrium order parameter for uniaxial systems. Moreover,

$$F_d = \frac{L_1}{2}\left(\frac{\partial Q_{ij}}{\partial x_k}\right)^2 + \frac{L_2}{2}\frac{\partial Q_{ij}}{\partial x_j}\frac{\partial Q_{ik}}{\partial x_k} + \frac{L_6}{2} Q_{lk}\frac{\partial Q_{ij}}{\partial x_l}\frac{\partial Q_{ij}}{\partial x_k}, \tag{10}$$

with

$$L_1 = \frac{1}{6\mathrm{S}_{eq}^2}[k_{33} - k_{11} + 3k_{22}]$$

$$L_2 = \frac{1}{\mathrm{S}_{eq}^2}[k_{11} - k_{22}]$$

$$L_6 = \frac{1}{2\mathrm{S}_{eq}^3}[k_{33} - k_{11}], \tag{11}$$

where $k_{11}$, $k_{22}$ and $k_{33}$ are the Frank elastic constants [3].

From variational principles, the balance of the energy variation is expressed as [31, 32]

$$\delta D + \delta \dot{F} = 0, \tag{12}$$

where $D$ is the Rayleigh dissipation function. Neglecting backflow [33], $D$ is given by

$$D = \int_V D dV = \int_V \gamma \, tr \dot{Q}^2 dV, \tag{13}$$

in which $D$ is the dissipation function density, $\gamma$ is related to the rotational viscosity, $V$ is the domain volume and the variation in the dissipation function density may be expressed by

$$\frac{\partial D}{\partial \dot{q}_i}\delta\dot{q}_i = 2\gamma \, tr\left(\dot{Q}\frac{\partial Q}{\partial q_i}\right)\delta\dot{q}_i. \tag{14}$$

Assuming summation over repeated indices, the generalised Euler–Lagrange equation, with suitable boundary conditions, gives the dynamic evolution of the system as solutions of the PDE equation system,

$$\frac{\partial D}{\partial \dot{q}_i}+\frac{\partial F_t}{\partial q_i}+\frac{\partial F_e}{\partial q_i}+\frac{\partial F_d}{\partial q_i}-\frac{\partial}{\partial x_j}\left(\frac{\partial F_d}{\partial q_{i,j}}\right) -\frac{\partial}{\partial x_j}\left(\frac{\partial F_e}{\partial q_{i,j}}\right)=0, \quad i=1,\ldots,5, \tag{15}$$

where the subscript $j$ denotes differentiation with respect to the spatial coordinates, $x_1$, $x_2$ and $x_3$. The equation governing the electric potential is given by

$$\nabla \cdot \boldsymbol{D} = \nabla \cdot [-\varepsilon_0 \boldsymbol{\varepsilon} \nabla \mathrm{U} + \boldsymbol{P}_S] = 0, \tag{16}$$

where $\boldsymbol{D}$ and $\varepsilon_0$ are the displacement field and the vacuum dielectric permeability, respectively, the dielectric tensor is expressed [18] as $\boldsymbol{\varepsilon} = \varepsilon_i \boldsymbol{I} + \varepsilon_a \boldsymbol{Q}$, and the spontaneous polarisation vector, $\boldsymbol{P}_s$, is instead expressed [34] as $P_S = \overline{e}\,[\nabla \cdot \mathrm{Q}]$.

Finally, the degree of biaxiality is given by the definition of its invariant measure [6],

$$\beta^2 = 1 - 6\frac{\mathrm{tr}\left[\mathrm{Q}^3\right]^2}{\mathrm{tr}\left[\mathrm{Q}^2\right]^3} \in [0,1]. \tag{17}$$

When $\beta^2 = 0$ the nematic texture is uniaxial, although the maximum value of biaxiality, $\beta^2 = 1$, corresponds to the biaxial nematic phase.

## 3. The adaptive grid method

The discretisation of the integration domain into an appropriate grid of mesh points typical of FEM procedure [19–20] is crucial in dealing with the type of problem we are dealing with. In one dimension, the problem can be tackled with a technique based on the *equidistribution principle* [29, 35], allowing control of the mesh map quality by equal distribution of a monitor function in each subinterval [27, 36–40]. The result is quite effective, since it allows an extremely accurate representation of sharp features such as shocks or defects. The optimal choice of the monitor function depends on the problem being solved, the numerical discretisation being used, and the norm of the error that has to be minimised [36–39].

If $u[z,t]$ is a solution over a physical domain $\Omega_\mathrm{p} = [0,1]$ of a PDE system, $z$ being the physical coordinate, introducing a fixed computational domain $\Omega_\mathrm{c} = [0,1]$ with $\xi$ computational coordinate, we may define a coordinate transformation

$$z = z[\xi, t], \xi \in \Omega_\mathrm{c}, t \in (0, \mathrm{T}], \tag{18}$$

from computational space $\Omega_\mathrm{c} \times (0,\mathrm{T}]$ to physical space $\Omega_\mathrm{p} \times (0,\mathrm{T}]$, and

$$\xi = \xi[z, t], z \in \Omega_\mathrm{p}, t \in (0, \mathrm{T}], \tag{19}$$

from physical space $\Omega_\mathrm{p}$ x (0,T] to computational space $\Omega_\mathrm{c}$ x (0,T], whereas Equation (18) represents a one-to-one mapping at time $t$ from computational to physical space. A uniform grid,

$$\xi_i = i/N, i = 0, 1, \ldots, N, \tag{20}$$

imposed on computational space, corresponds to a set of nodes in physical space:

$$0 = z_0[t] < z_1[t] < \ldots z_N[t] = 1. \tag{21}$$

The mesh map quality is controlled by an equal distribution of the monitor function, $M[u[z,t]]$, over each subinterval. A mesh equidistributes the monitor function, $M[u[z,t]]$, if

$$\int_{zi-1[t]}^{zi[t]} M[u[s,t]]\,ds = \frac{1}{N}\int_0^1 M[u[s,t]]ds. \tag{22}$$

Generalising over the integration domain,

$$\int_0^{z[\xi,t]} M[u[s,t]]\,ds = \xi \int_0^1 M[u[s,t]]ds, \tag{23}$$

which is the integral form of the equidistribution principle. The coordinate mapping $z[\xi,t]$ can be determined by differentiating Equation (23) with respect to $\xi$, giving the mesh equation

$$M[z[\xi,t]]\frac{\partial}{\partial \xi}\mathrm{z}[\xi,t] = \int_0^1 M[u[s,t]]ds = C[t]. \tag{24}$$

In order to keep the equidistribution of the monitor function constant over the integration domain, a larger value of the monitor function corresponds to a denser mesh.

The choice of the monitor function is fundamental for controlling the quality of the mesh and final convergence of the FEM solution [27, 29, 36–39]. We have demonstrated [28] that an appropriate choice for the geometry of our domain is the monitor function introduced by Beckett *et al*. [29], described below as the BM monitor function,

$$M[u[z,t]] = \alpha + \sqrt{\left|\frac{\partial u[z,t]}{\partial z}\right|}, \tag{25}$$

where

$$\alpha = \int_0^1 \sqrt{\left|\frac{\partial u[z,t]}{\partial z}\right|}\,dz. \tag{26}$$

This has the advantage of being self-regulating, since the $\alpha$ parameter used to set the floor arises by integration over the entire spatial domain. Moreover, the mesh adaptivity is controlled through the $\alpha$ parameter at each time step, and therefore has no need for external intervention.

Error and convergence analysis are beyond the scope of the present paper, but Beckett *et al*. [29] have demonstrated that for one-dimensional problems an optimal convergence rate of dynamical adaptive solutions can be reached when algorithms based on the BM monitor function are used. The overall adaptive solution of our multidimensional time-dependent problem is an iterative process involving two separate steps: (i) a mesh generation using the equidistribution principle based on the numerical solution at the current time step; and (ii) the solution of the PDEs on the newly generated grid, and then time updated. The second step in particular involves an iteration process based on relaxation methods [41], in which the LC free energy at each time step is minimised to update the $\boldsymbol{Q}$ profile, and this in turn is used to update the electric potential profile. The stability of the iterative updating relies on proper selection of the updating time step, $\Delta t$ [42], at which the solution of our PDE system, Equation (15), is calculated using FEM. To overcome the difficulty related to the non-linearity, we have used the Galerkin method, associated with a weak formulation of the residual of the differential equations [19–20], interpolating the local $\boldsymbol{Q}$ distribution in each element by quadratic shape functions. Once the $\boldsymbol{Q}$ distribution has been determined, the potential distribution is calculated by solving Equation (16) by Ritz's method [13]. It should be born in mind that, since our problem is modelled by six coupled PDEs solved simultaneously, at each time step we have six unknown exact solutions $u[z,t]$, five of which refer to each Lagrangian parameter $q_i$, $i\in[1,5]$, and one to the electric potential solution within the cell. We have developed the following algorithm [28]:

(1) A uniform initial grid $z_j[0]$ is generated and the corresponding initial solution $u_j[0]$ is calculated using FEM:
*a temporal loop is done in the time domain updating mesh and solution u, putting forward PDEs:*
**while** $t_n < T$
*the mesh is redistributed in a few steps* $\nu \geq 0$*:*
**do**

(2) The monitor function is evaluated, the grid is moved from $z_j[\nu]$ to $z_j[\nu+1]$ with an iterative procedure so that the monitor function is equally distributed in each subinterval, and a solution $u_j[\nu+1]$ is calculated on the new mesh
**until** $\nu \leq \nu_{max}$

(3) The PDE system is put forward on the new mesh $z_j[\nu+1]$ to obtain a numerical approximation $u_j[\nu+1]$ at the new time level $t_{n+1}$:
**end**.

At time $t = 0$ the grid is uniformly distributed, and Equations (15) and (16) are solved at the current time. Step (ii) and the advance in time of the solution were carried out using the COMSOL Multiphysics$^{TM}$ finite element package with Matlab$^{TM}$ [43]. At each time step the problem was solved by minimising the energy density functional, and the solution $u$ was then used to update the monitor function.

## 4. The modelled cell

Investigations on the $\pi$-cell, a sandwich cell in which the molecular director can rotate by about 180° through the cell [44], demonstrate the possibility of obtaining nematic transitions between two textures having different topologies, for instance between a splayed and a $\pi$-bend / $\pi$-twist [6]. These rapid textural changes can be obtained by bulk order reconstruction, a phenomenon that allows the director reorientation between two perpendicular directions without macroscopic rotation of the director itself.

In the splay configuration, Figure 1(a), the nematic director lies almost parallel to the boundary plates, with a slightly splayed deformation, whereas in the $\pi$-bent state, Figure 1(c), the nematic is almost perpendicular to the plates and presents a bend deformation which is topologically equivalent to a twisted configuration. Depending on the tilt angle and the ratio of the elastic moduli, either of these states could have a lower elastic energy, but the topological energy barrier between them prevents spontaneous elastic relaxation. The switching is only possible by breaking the planar nematic wall present in the centre of the cell, Figure 1(b), and then reconstructing the new nematic texture with or without $\pi$-torsion. In principle, this can be achieved by moving defects, by anchoring breaking [45, 46] or by melting the nematic order in a plane [6, 47]. In practice, the nematic biaxial order reconstruction induced by the electric field is a mechanism that enables escape from topological constraints and requires less energy than full melting.

We have modelled the physical problem using a one-dimensional $\pi$-cell of thickness $d = 1$ μm, with a strong anchoring energy on both boundary surfaces. In particular, the pre-tilt angles are $\theta_L = 19°$ on the lower surface and $\theta_U = -19°$ on the upper surface, both measured with respect to the plates. This configuration allows the initial splay texture to vary the direction of **n** between $-19°$ and 19° along the thickness of the cell. We applied an electric pulse at right

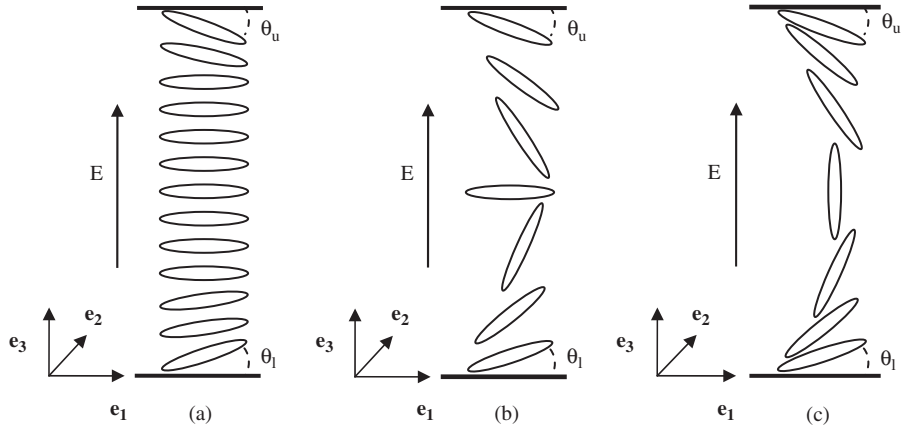


Figure 1. Physical geometry of the $\pi$-cell with nematic molecules in different states: (a) horizontal alignment with a slight splay; (b) intermediate state, with a thin wall in the centre; (c) mostly vertical alignment.

angles to the plates, i.e. along the $z$-axis, starting at time $t = 0$ s for a duration of $\tau = 0.25$ ms, setting its amplitude to 10, 11, 12, 13 and 14 V $\mu$m$^{-1}$.

The one-dimensional cell is discretised by a mesh of 285 grid points, and the dynamic evolution of the $\boldsymbol{Q}$ tensor is monitored by sampling the time interval at a time step of magnitude, $\delta t = 0.1$ $\mu$s. We have recently [28] carried out an initial analysis of the numerical method used in the present study and we reported that 285 grid points represented the best compromise between spatial resolution and computational effort for the system under study. Other computations performed on the same system using a uniform grid required up to 1000 grid points in order to achieve a solution accuracy comparable with the reported results. A similar conclusion had been obtained by Ramage and Newton [27], using a FEM–MMPDE model implemented with an AL monitor function, supporting the numerical results obtained by Barberi *et al*. [6] by finite difference discretisation. The solution of the problem is obtained through the iterative procedure already described [28], in which at each time step an adaptive mesh is generated, evaluating the monitor function which allows the mesh generated from the previous nematic configuration to be moved. Secondly, the PDE system, Equations (15) and (16), is evaluated in order to generate the new nematic configuration as input for the following time step. At $t = 0$ s the grid points are uniformly distributed and the $\boldsymbol{Q}$ tensor profile is preset by the boundary conditions.

Equations (15) and (16) are solved for each time step, replacing in Equations (25) and (26) the exact solution $u[z,t]$ with $\mathrm{tr}[\boldsymbol{Q}^2]$, since it is the sum of the squared $\boldsymbol{Q}$ eigenvalues which varies rapidly in the frustrated region where the degree of order is not constant. The typical physical parameters for a 4-cyano-4′-*n*-pentylbiphenyl (5CB) nematic LC at $\Delta T = -1$°C [48] are used, with a biaxial coherence length $\xi_b$ of about ten nanometers. Since we do not *a priori* know either whether biaxial transition will take place, nor where it may possibly take place, in order to characterise the dynamical evolution of the $\boldsymbol{Q}$ tensor we monitored the biaxiality, Equation (17), arising inside the whole cell. We also computed the current density flowing through the cell during the application of the electric fields, neglecting ionic effects, since nematics are considered to be purely dielectric materials [6].

## 5. Numerical results

Figure 2 shows the dynamical evolution of biaxiality arising inside the cell over time interval, $0 \text{ s} \leq t \leq 1 \times 10^{-4}$ s, for a range of electric field amplitudes, (a) 10 V $\mu$m$^{-1}$, (b) 11 V $\mu$m$^{-1}$, (c) 12 V $\mu$m$^{-1}$, (d) 13 V $\mu$m$^{-1}$ and (e) 14 V $\mu$m$^{-1}$. The biaxial order varied between zero for a uniaxial nematic texture (black colour), and 1 for a biaxial nematic texture (white colour), and the other values shown are linearly mapped from a grey scale between zero and 1.

In the starting nematic texture, $t = 0$ s, the molecules are in a splayed configuration compatible with the prescribed boundary conditions, as illustrated in Figure 1(a), and the biaxiality is very weak. Applying at $t > 0$ s an electric pulse of amplitude 10 V $\mu$m$^{-1}$, the nematic molecules tend to align along the electric field. The nematic director is almost everywhere perpendicular to the plates, apart from three regions: in the centre of the cell, where the molecules remain parallel to the boundary plates, Figure 1(b) [6, 13, 28], and in the two thin surface layers where the nematic material is forced by the strong anchoring conditions to retain its initial orientation. Accordingly, the biaxiality within the bulk remains practically zero, apart from the two symmetrical biaxial walls close to the boundary plates and over a thin region in the

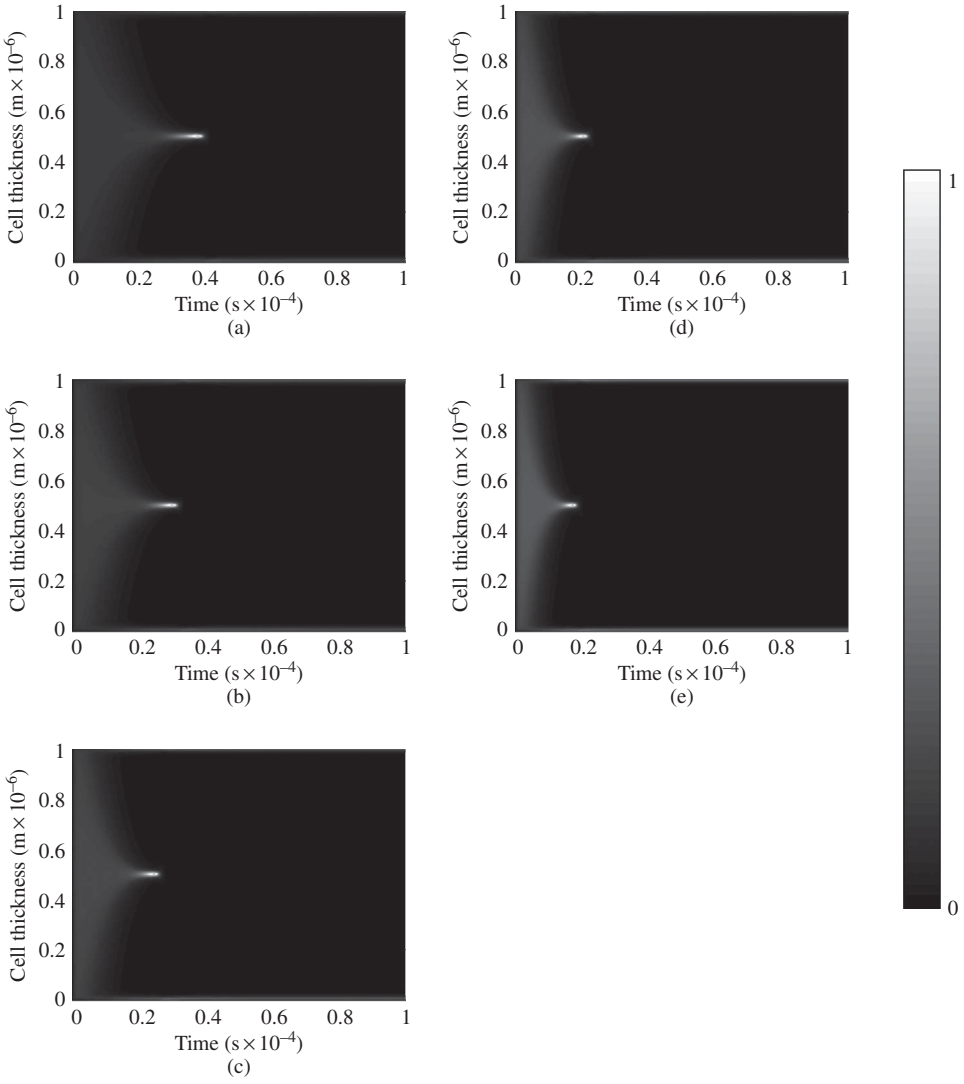


Figure 2. Surface contour plots of the biaxial order evolution in the 0 ms $\leq t \leq$ 0.1 ms time interval for electric pulse amplitudes of 10 V $\mu$m$^{-1}$ (a), 11 V $\mu$m$^{-1}$ (b), 12 V $\mu$m$^{-1}$ (c), 13 V $\mu$m$^{-1}$ (d) and 14 V $\mu$m$^{-1}$ (e), linearly mapped in a grey level scale between black (zero biaxiality) and white (maximum biaxiality).

centre of the cell where almost all the nematic distortion is concentrated, see Figure 2(a). In the latter area the maximum frustration occurs, and a biaxial *wall* of thickness comparable with $\xi_b$ occurs, connecting the homeotropic nematic textures with the planar nematic orientation located at the centre of the cell. The biaxiality reaches its maximum just before the splay–bend transition, whereas soon after the transition is completed the initial splay texture is replaced by a bend texture, as shown in Figure 1(c). Thus, the transient bulk biaxial wall allows the topological barrier connecting these two different nematic textures to be overcome.

Figure 3(a), which is a magnified version of Figure 2(a) at the point around $t = 40$ $\mu$s, shows the transition from splay to bend mediated by the biaxial wall [13]. The maximum biaxiality occurs in a ring, still comparable with $\xi_b$ in size, and corresponds to a purely biaxial state in which one of the eigenvalues of the order tensor vanishes [6, 49]. In the centre of the ring the biaxiality is zero, corresponding to a pure uniaxial state in which the two eigenvalues of the order tensor are equal and positive. The temporal evolution of the biaxial order induced by the electric field is the dynamic equivalent of the spatial order evolution within a defect [13, 14].

Our proposed adaptive grid algorithm moves the nodes towards the regions of high gradient of $\boldsymbol{Q}$ at the centre and the two surface layers of the cell, in order to capture the relevant nematic distortion which occurs in the spatial domain during the application of the electric field. The effective clustering of grid points in the

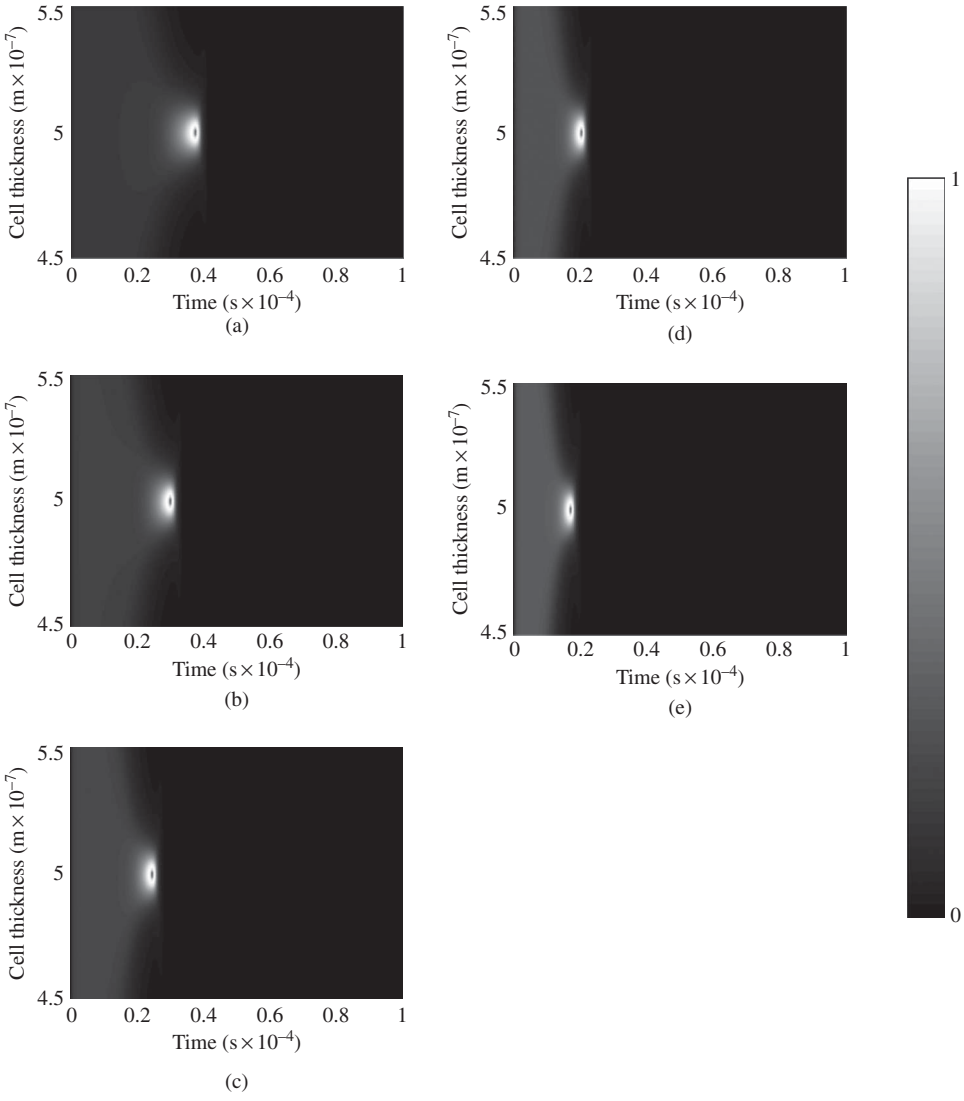


Figure 3. Magnification of Figure 2, showing the splay–bend transition mediated by the biaxial wall.

regions where they are needed permits smaller variation in the $\boldsymbol{Q}$-tensor [28]. On increasing the amplitude of the electric field the transition becomes monotonically faster, Figures 2(b)–(d) and 3(b)–(d), and finally, at an amplitude of 14 V $\mu m^{-1}$ it is completed within 20 $\mu$s, Figures 2(e) and 3(e).

The dynamic profile of biaxiality indicates the occurrence of strong topological variations within the $\pi$-cell induced by the applied electric field, and since the current flowing across the cell involves all the nematic material, it is expected to carry information sensitive with respect to such variations. On the other hand, in experiments conducted on a cell containing a 5CB nematic liquid crystal subjected to a strong electric field [7–9], it has been seen that the current flowing across the cell can be measured with better temporal resolution than other techniques available for measurement of birefringence.

Figure 4 shows the calculated electric current which flows across the cell during the application of electric pulses. Curve (a) refers to the electric response of the cell when a pulse of amplitude 10 V $\mu m^{-1}$ is applied; the first broad structure is related to the dielectric molecular reorientation along the field direction, while the second peak is associated with the vanishing nematic order in the thin biaxial wall [6, 12, 13]. Increasing the amplitude of the electric pulse, the current undergoes some changes, shown by curves (b)–(e) in Figure 4. Due to the elastic response of the nematic system, the peak related to the dielectric reorientation becomes sharper and faster, while the order reconstruction peak, according to the occurrence of the splay–bend transition (see Figures 2 or 3 for comparison), takes place sooner. In addition, the order reconstruction peak is well resolved at lower pulse amplitudes, whereas at higher values it becomes

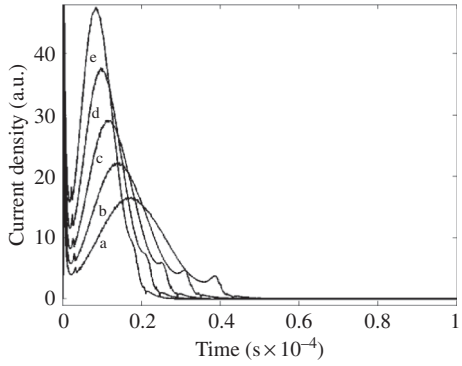


Figure 4. Plot of the electric current density flowing across the cell in the 0 ms $\leq t \leq$ 0.1 ms time interval for applied electric field amplitudes of 10 V $\mu$m$^{-1}$ (a), 11 V $\mu$m$^{-1}$ (b), 12 V $\mu$m$^{-1}$ (c), 13 V $\mu$m$^{-1}$ (d) and 14 V $\mu$m$^{-1}$ (e).

superimposed over the tail of the first peak. In fact, in curve (a), at 10 V $\mu$m$^{-1}$ it is centred at 38.5 $\mu$s, then moving to about 31 $\mu$s, curve (b), to 25 $\mu$s (c), 21 $\mu$s (d) and to 17.5 $\mu$s in curve (e), for pulse amplitudes of 11 V $\mu$m$^{-1}$, 12 V $\mu$m$^{-1}$, 13 V $\mu$m$^{-1}$and 14 V $\mu$m$^{-1}$, respectively. If the applied pulse voltage is too strong, the electrical response due to the order reconstruction is hidden within the dielectric peak and it becomes impossible to distinguish the transition, even experimentally [7–9].

Since we employed strong anchoring energy at the boundary surfaces, the application of the electric field induced a surface elastic distortion which tended to be relaxed by the biaxiality arising at the surface of the liquid crystal layer [50, 51].

Figure 5 shows a magnification of the computed biaxiality close to the upper boundary surface layer for different electric pulse amplitudes; for reasons of symmetry the effect is also identical at the lower boundary surface layer. The vertical axis corresponds to the cell thickness in the range, $0.985 \times 10^{-6}$ m $\leq z \leq 1 \times 10^{-6}$ m, while the horizontal axis corresponds to the time scale of the solution evolving in the 0 s $\leq t \leq 1 \times 10^{-4}$ s interval.

Figure 5(a) shows the biaxiality evolving close to the boundary surface when an electric pulse of amplitude 10 V $\mu$m$^{-1}$ is applied. In this case the nematic molecules are subject to two different stresses; on the one hand the electric field tends to align the nematic molecules along the $z$-axis, and on the other the strong anchoring energy imposed serves to keep them aligned in this direction. This elastic competition causes a high degree of frustration to be located close to the bounding surface, where a biaxial layer of thickness comparable to the biaxial coherence length $\xi_b$ grows in order to relax the strong distortional effect. During the application of the electric field the surface biaxiality is reasonably uniform, and it does not vanish, as instead occurs in the centre of the cell. In fact, the

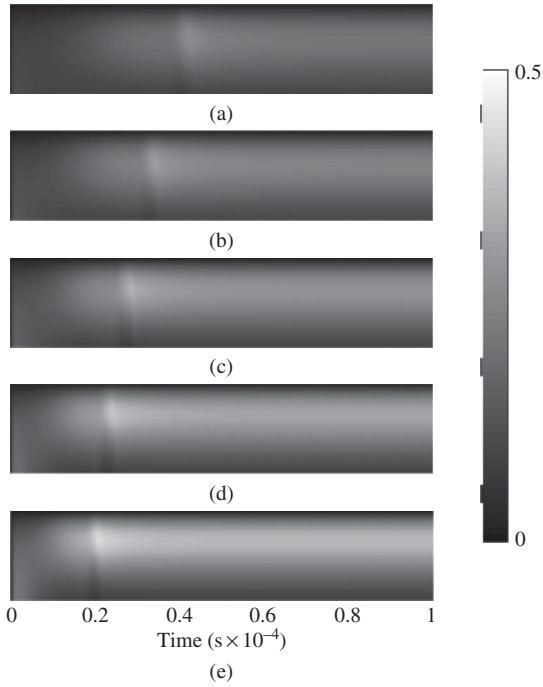


Figure 5. Map of the biaxiality in a region 15 nm thick, close to the upper boundary plate of the $\pi$-cell, for applied electric field amplitudes of 10 V $\mu$m$^{-1}$ (a), 11 V $\mu$m$^{-1}$ (b), 12 V $\mu$m$^{-1}$ (c), 13 V $\mu$m$^{-1}$ (d) and 14 V $\mu$m$^{-1}$ (e). Compared to Figure 2, the map is magnified twofold. For each panel, the vertical axis corresponds to the cell thickness in the range $0.985 \times 10^{-6}$ m $\leq z \leq 1 \times 10^{-6}$ m, while the horizontal axis corresponds to the time scale of the solution evolution in a 0 ms $\leq t \leq$ 0.1 ms time interval.

order reconstruction takes place when two orthogonal nematic orientations are in competition at the same location. On the other hand, the nematic is affected on the surface by the vertical orientation imposed by the electric field and the oblique orientation given by the anchoring, and the surface order reconstruction does not occur [49–52]. Increasing the pulse amplitude from 11 V $\mu$m$^{-1}$ to 14 V $\mu$m$^{-1}$, see Figures 5(b)–5(e), increases the nematic surface strain induced, and the moving mesh technique is able to cluster the nodes near the surface layer, at which the nematic distortion is relaxed due to the nematic biaxial states induced. The signature of the movement of the nodes can be observed by examining the biaxial spikes shown in Figures 5(b)–5(e).

## 6. Conclusions

In this study we have applied a moving mesh partial differential equation finite element method to a dynamic $\boldsymbol{Q}$-tensor model, for a nematic liquid crystal confined in a cell with symmetrical anchoring conditions. We have simulated the temporal evolution of both biaxility and the current flowing within the cell. Our computations show that the order reconstruction

phenomenon is strongly dependent on the amplitude of the electric pulse applied across the $\pi$-cell. In particular, the dynamic $\boldsymbol{Q}$-tensor profile indicates that the formation of the biaxial wall, growing at the centre of the cell to connect topologically the non-equivalent nematic textures, becomes more rapid on increasing the pulse amplitude. In addition, the biaxiality close to the bounding plates is influenced by surface effects. The current computations during the application of the fields are particularly sensitive to the textural changes occurring within the $\pi$-cell. The temporal position of the current peaks at a given amplitude of the applied electric field depends on the elastic response of the nematic system to the electric stress, and precisely locates the splay–bend transition.

The numerical method employed allows detailed computations of the $\boldsymbol{Q}$-tensor dynamics of nematics to be performed, emphasising its benefits. Since the spatial position at which the biaxial wall increases is *a priori* unknown, the moving mesh method reduces the use of a huge number of grid points required, replacing them with uniform discretisations to resolve the finer details of the variations in the order tensor. In the moving mesh method the grid points are relocated according to the variations in biaxial distortion, and the numerical simulation is thus driven by the gradient of the order tensor. As a consequence, a smaller number of grid points is thus required than for uniform grids, which reduces the computational cost and increases the overall resolution. In fact, the detailed computation of both biaxiality and electric current density across the cell allows a distinction to be made between bulk- and surface-related contributions to the $\boldsymbol{Q}$-tensor dynamics.



## References


[1] Oseen, C.W. *Trans. Faraday Soc*. **1933**, *29*, 883–889.
[2] Franck, F. *Discuss. Faraday Soc*. **1958**, *25*, 19–28.
[3] de Gennes, P.G.; Prost, J. *The Physics of Liquid Crystals*; Clarendon Press: Oxford, UK, 1993.
[4] Barberi, R.; Durand, G. In *Handbook of Liquid Crystal Research*: Collings, P.J., Patel, J.S., Eds.; Oxford University Press: New York, 1997; Ch. 6.
[5] Carbone, G.; Lombardo, G.; Barberi, R.; Musevic, I.; Tkalec, U. *Phys. Rev. Lett.* **2009**, *103*, 167801–4.
[6] Barberi, R.; Ciuchi, F.; Durand, G.; Iovane, M.; Sikharulidze, D.; Sonnet, A.; Virga, E. *Eur. Phys. J. E* **2004**, *13*, 61–71.
[7] Barberi, R.; Ciuchi, F.; Lombardo, G.; Bartolino, R.; Durand, G.E. *Phys. Rev. Lett*. **2004**, *93*, 137801–4.
[8] Joly, S.; Dozov, I.; Martinot-Lagarde, P. *Phys. Rev. Lett*. **2006**, *96*, 019801.
[9] Barberi, R.; Ciuchi, F.; Lombardo, G.; Bartolino, R.; Durand, G.E. *Phys. Rev. Lett.* **2006**, *96*, 019802.
[10] Ciuchi, F.; Ayeb, H.; Lombardo, G.; Barberi, R.; Durand, G.E. *Appl. Phys. Lett*. **2007**, *91*, 244104–3.
[11] Ayeb, H.; Ciuchi, F.; Lombardo, G.; Barberi, R. *Mol. Cryst. Liq. Cryst*. **2008**, *481*, 73–79.
[12] Lombardo, G.; Ayeb, H.; Ciuchi, F.; De Santo, M.P.; Barberi, R.; Bartolino, R.; Virga, E.G.; Durand, G.E. *Phys. Rev. E: Stat., Nonlinear, Soft Matter Phys.* **2008**, *77*, 020702–4.
[13] Lombardo, G.; Ayeb, H.; Barberi, R. *Phys. Rev. E: Stat., Nonlinear, Soft Matter Phys.* **2008**, *77*, 051708–10.
[14] Schopohl, N.; Sluckin, T.J. *Phys. Rev. Lett.* **1987**, *59*, 2582–2584.
[15] Ambrožič, M.; Kralj, S.; Virga, E.G. *Phys. Rev. E: Stat., Nonlinear, Soft Matter Phys.* **2007**, *75*, 031708–9.
[16] de Gennes, P. *Phys. Lett*. **1969**, *30A*, 454–455.
[17] Virga, E.G. *Variational Theories for Liquid Crystals*; Chapman and Hall: London, 1994.
[18] Anderson, J.E.; Watson, P.E.; Bos, P.J. *LC3D: Liquid Crystal Display 3-D Directory Simulator, Software and Technology Guide*; Artech House: Boston, MA, USA, 1999.
[19] Zienkiewicz, O.; Taylor, R. *The Finite Element Method*; Butterworth–Heinemann: Oxford, 2002; Vol. 1.
[20] Known, Y.; Bang, H. *The Finite Element Method using Matlab*; CRC Press: Boca Raton, FL, USA, 2000.
[21] Tang, T. *Contemp. Math*. **2005**, *383*, 141–173.
[22] Haegland, B.; Skaflestad, B. *Preprint Numerics No. 2/2002*; Norwegian University of Science and Technology: Trondheim, Norway, 2002.
[23] N. Acikgoz. Ph.D. Thesis, Georgia Institute of Technology, USA, 2007.
[24] Barrett, J.W.; Feng, X. Prohl, A. *Math. Model. Anal*. **2006**, *40*, 175–199.
[25] Patricio, P.; Tasinkevych, M.; Telo da Gama, M.M. *Eur. Phys. J. E* **2002**, *7*, 117–122.
[26] James, R.; Willman, E.; Fernández, F.A. *IEEE Trans. Electron. Devices* **2006**, *53*, 1575–1582.
[27] Ramage, A.; Newton, C.J.P. *Liq. Cryst*. **2007**, *34*, 479–487.
[28] Amoddeo, A.; Barberi, R.; Lombardo, G. *Computers and Mathematics with Applications* **2010**, *60*, 2239–2252.
[29] Beckett, G.; Mackenzie, J.A.; Ramage, A.; Sloan, D.M. *J. Comput. Phys*. **2001**, *167*, 372–392.
[30] Huang, W.; Ren, Y.; Russell. R.D. *Siam. J. Numer. Anal*. **1994**, *31*, 709–730.
[31] Sonnet, A.; Maffettone, P.; Virga, E. *J. Non-Newtonian Fluid Mech*. **2004**, *119*, 51–59.
[32] Sonnet, A.; Virga, E. *Phys. Rev. E: Stat., Nonlinear, Soft Matter Phys.* **2001**, *64*, 031705–10.
[33] Brimicombe, P.D.; Raynes, E.P. *Liq. Cryst*. **2005**, *32*, 1273–1283.
[34] Alexe-Ionescu, A. *Phys. Lett. A* **1993**, *180*, 456–460.
[35] de Boor, C. In *Conference on the Applications of Numerical Analysis, Dundee 1973*: Morris, J., Ed.; Vol. 363 of Lecture Notes in Mathematics; Springer–Verlag: Berlin, 1974; pp 12–20.
[36] Pereyra, V.; Sewell, E.G. *Numer. Math*. **1975**, *23*, 261–268.
[37] Russell, R.D.; Christiansen, J. *J. Siam. J. Numer. Anal*. **1978**, *15*, 59–80.
[38] White, A.B. *Siam. J. Numer. Anal*. **1979**, *16*, 472–502.
[39] Beckett, G.; Mackenzie, J.A. *Appl. Numer. Math*. **2000**, *35*, 87–109.
[40] Huang, W.J. *Comput. Phys*. **2001**, *171*, 753–775.
[41] Biscari, P.; Peroli, G.; Sluckin, T. *Mol. Cryst. Liq. Cryst. A* **1997**, *292*, 91–101.
[42] Anderson, J.; Titus, C.; Watson, P.; Bos, P. *SID Int. Symp. Dig. Tec*. **2000**, *31*, 906–909.

[43] COMSOL Multiphysics™, http://www.comsol.com/; Matlab™, http://www.mathworks.com.
[44] Alexe-Ionescu, A.L.; Barberi, R.; Giocondo, M.; Cnossen, G.; van der Donk, T.H. *Appl. Phys. Lett*. **1995**, *66*, 1701–3.
[45] Barbero, G.; Barberi, R. *J. de Physique* **1983**, *44*, 609–616.
[46] Dozov, I.; Nobili, M.; Durand, G. *Appl. Phys. Lett*. **1997**, *70*, 1179–1181.
[47] Martinot-Lagarde, P.; Dreyfus-Lambez, H.; Dozov, I. *Phys. Rev. E: Stat., Nonlinear, Soft Matter Phys.* **2003**, *67*, 051710–4.
[48] Ratna, B.; Shashidhar, R. *Mol. Cryst. Liq. Cryst*. **1977**, *42*, 113–125.
[49] Kralj, S.; Virga, E.G.; Žumer, S. *Phys. Rev. E: Stat., Nonlinear, Soft Matter Phys.* **1999**, *60*, 1858–1866.
[50] Ayeb, H.; Lombardo, G.; Ciuchi, F.; Hamdi, R.; Gharbi, A.; Durand, G.; Barberi, R. *App. Phys. Lett*. **2010**, *97*, 104104–3.
[51] Lombardo, G.; Ayeb, H.; Ridha, H.; Cosenza, F.; Barberi, R. (unpublished).
[52] Ambrožič, M.; Bisi, F.; Virga, E.G. *Continuum Mech. Therm*. **2008**, *20*, 193–218.